

Brightness and Fluctuation of the Mid-Infrared Sky from *AKARI* Observations towards the North Ecliptic Pole

Jeonghyun Pyo¹, Toshio Matsumoto^{2,3}, Woong-Seob Jeong¹, and Shuji Matsuura³

¹Korea Astronomy and Space Science Institute (KASI), Daejeon 305-348, Republic of
Korea

²Department of Physics and Astronomy, Seoul National University, Seoul 151-742,
Republic of Korea

³Institute of Space and Astronautical Science (ISAS), Japan Aerospace Exploration
Agency (JAXA), Kanagawa 252-5210, Japan

Received _____; accepted _____

ABSTRACT

We present the smoothness of the mid-infrared sky from observations by the Japanese infrared astronomical satellite *AKARI*. *AKARI* monitored the north ecliptic pole (NEP) during its cold phase with nine wavebands covering from 2.4 to $24\,\mu\text{m}$, out of which six mid-infrared bands were used in this study. A simple sinusoidal fit to the seasonal variation of the sky brightness shows that the mid-infrared brightness towards the NEP is not affected by small-scale features of the interplanetary dust cloud. We applied power spectrum analysis to the images in order to search for the fluctuation of the sky brightness. Observed fluctuation is explained by fluctuation of photon noise, shot noise of faint sources, and Galactic cirrus. The fluctuations at a few arcminutes scales at short mid-infrared wavelengths (7, 9, and $11\,\mu\text{m}$) are largely caused by the diffuse Galactic light of the interstellar dust cirrus. At long mid-infrared wavelengths (15, 18, and $24\,\mu\text{m}$), photon noise is the dominant source of fluctuation over the scale from arcseconds to a few arcminutes. The residual fluctuation power at $200''$ after removing these contributions is at most $1.08 \pm 0.22\,\text{nW m}^{-2}\text{sr}^{-1}$ or 0.05% of the brightness at $24\,\mu\text{m}$ and at least $0.52 \pm 0.13\,\text{nW m}^{-2}\text{sr}^{-1}$ or 0.02% at $18\,\mu\text{m}$. We conclude that the upper limit of the fluctuation in the zodiacal light is 0.02% of the sky brightness.

Subject headings: infrared: diffuse background

1. Introduction

Fluctuation in infrared sky brightness has been measured for various purposes depending on the wavelength regime. In the near-infrared, researchers have tried to discriminate the fluctuation by the cosmic near-infrared background (CNIRB) from those by other foreground sources. The CNIRB is believed to originate from the light of first (Population III) stars, which reionized the Universe (Santos et al. 2002). Recently, Matsumoto et al. (2011) found excess fluctuation in the scale larger than $\sim 100''$ from the *AKARI* north ecliptic pole (NEP) survey at 2.4, 3.2, and $4.1\,\mu\text{m}$ and interpreted it as CNIRB fluctuation. Their results are consistent with independent fluctuation measurements from the *Spitzer* observations (Kashlinsky et al. 2005, 2007). In the far-infrared, the Galactic cirrus of interstellar dust is a prominent source of diffuse brightness and fluctuation. Far-infrared fluctuation measurements are used for studies of not only the Galactic cirrus but also the clustering of unresolved, high-redshift objects. The fluctuation by the cosmic far-infrared background has also been reported by several researchers (see Jeong et al. 2007; Matsuura et al. 2011, and references therein).

The zodiacal light (ZL) is a conspicuous probable source of infrared fluctuation, because it dominates the sky brightness over a wide wavelength range of the infrared (Leinert et al. 1998). Ábrahám et al. (1997) analyzed five $0.5^\circ \times 0.5^\circ$ images from $25\,\mu\text{m}$ observations of the Infrared Space Observatory (ISO) and concluded that the upper limit of the ZL fluctuation is 0.2% of brightness, which corresponds to $\sim 5\,\text{nW m}^{-2}\text{sr}^{-1}$ towards the NEP. However, the ISO observation had a sparse resolution of $3'$ and the 0.2% fluctuation is apparently too large when compared with modern CNIRB fluctuation measurements.

In this paper we make use of the *AKARI*'s NEP monitor observations in six mid-infrared wavebands to measure the fluctuations in the sky brightness. We will concentrate on searching for residual fluctuation at around $200''$ scale after eliminating the contributions

from known fluctuation sources. Section 2 introduces the details of the observations and the image reduction and calibration processes. In Section 3, we attempt sinusoidal fits to the seasonal variation of the sky brightness to check whether the observations were affected by the substructures of the interplanetary dust (IPD) cloud. Section 4 shows the results from the fluctuation analysis and Section 5 discusses them. We summarize the paper in Section 6.

2. Observations and Data Reduction

2.1. Monitor Observations

AKARI rotates around the Earth along a Sun-synchronous polar orbit of an altitude of 700 km (Murakami et al. 2007). Owing to frequent opportunities to observe the NEP over the whole mission period, it observed regions close to the NEP twice a month in order to check the detectors’ stability (Tanabé et al. 2008) and to study the CNIRB (Matsumoto et al. 2011). The Monitor Fields were observed with an Infrared Camera (IRC) composed of three channels, NIR, MIR-S, and MIR-L. Each channel is equipped with three photometric bands. In this paper, we will focus on the two mid-infrared channels, MIR-S and MIR-L. Table 1 lists the imaging specifications of IRC MIR-S and MIR-L channels and bands (Onaka et al. 2007; Lorente et al. 2008). With six mid-infrared bands, the IRC covers a wavelength range from 7 to $24\,\mu\text{m}$.

The monitor observation lasted from June 2006 to August 2007. Because *AKARI* suffered from the impact of scattered Earth-shine during the northern hemisphere’s summer season (Verdugo et al. 2007; Pyo et al. 2010), however, we excluded the observations in that period. Table 2 lists the pointed observations¹ used in this paper and Figure 1 shows

the observed fields in the ecliptic coordinates. Note that the fields of MIR-L channel rotated around those of the MIR-S channel due to the different off-axis positions among the channels in the focal plane: The field-of-view of the MIR-L channel is about 20' away from that of MIR-S (Onaka et al. 2007).

2.2. Data Reduction

The observation data is reduced with the *AKARI* IRC Image Data Reduction Pipeline² (version 20091022). To correct the dark currents in the exposure frames, the reduction pipeline by default subtracts the super-dark frames generated from the dark current measurements in the Large Magellanic Cloud observations (Lorente et al. 2008). For our analysis, we modified the pipeline and subtracted the dark frame taken just before exposures in each pointed observation, the so-called self-dark. This modification mitigated the effect of the dark-current variation over long-term in the exposure frames (Lorente et al. 2008).

AKARI provides IRC observers with five observation modes, the so-called Astronomical Observation Templates (AOTs). We selected AOT IRC03, which enabled us to obtain images in nine bands with a single pointed observation including the near-infrared channel. The near-infrared images simultaneously taken with MIR-S and MIR-L were separately studied by Matsumoto et al. (2011). In the IRC03 template, we have two or three exposures for each mid-infrared band, each of which consisted of one short-exposure (0.5844 second) and three long-exposure (16.3632 second) frames (Onaka et al. 2007). We excluded

¹The observation data is available on the *AKARI* homepage (<http://darts.isas.jaxa.jp/astro/akari>) of the ISAS/JAXA Data Archives and Transmission System (DARTS) by querying with the observation IDs.

²Available in the *AKARI* Observers Page (<http://www.ir.isas.jaxa.jp/ASTRO-F/Observation/>).

short-exposure frames due to their low signal-to-noise ratio. On the other hand, the long-exposure (LE) frames suffered from after-effects. The second and third LE frames show systematically larger electron counts than the first (LE1) does, and are ignored. For the MIR-S bands, the LE1 frames in later exposures are also ignored, because they are systematically brighter than the one in the first exposure. In the case of the MIR-L bands, the situation is more complicated. The L18W band comes first in the sequence of the MIR-L channel exposures and the electron count is the largest in that band. The first L18W-band exposure significantly affects the following first L15- and L24-band exposures, which record higher counts than the second ones do. Therefore, we took the LE1 frames in the second exposures of the L15 and L24 bands, while the LE1 frame in the first exposure was chosen for the L18W band. Consequently, only one image was taken for each band from every pointed observation.

Parts of images affected by internal lamps and bright lines of pixels were masked out. Additionally, we masked the left half of the MIR-L channel frames, in which a pattern of internally scattered light was significant. The regions used in the analysis are shown in Figure 2.

The stars in the images were removed by masking the pixels whose values were larger than or smaller than three times the standard deviation with respect to the average, along with 3×3 pixels surrounding them. The masking was repeated until there remained no more pixels to be clipped. The fractions of the masked pixels were $\lesssim 6\%$ for the MIR-S bands, $\sim 9\%$ for the L15 and L18W bands, and $\sim 11\%$ for the L24 band. We did not combine the reduced images to investigate the seasonal variation of the brightness.

The dark frames were processed in the same way as the exposure frames except that we skipped the dark subtraction procedure. After the whole reduction processes, we obtained the average image of the dark frames for each channel and subtracted it from

individual dark frames to strip the large-scale patterns in the dark current. The patterns were especially significant in the MIR-S channel dark frames and had an impact on the fluctuation measurements in the scale larger than about $50''$. These large-scale patterns were suppressed in the exposure frames when subtracting the dark frames from them pixel by pixel.

2.3. Absolute Calibration

We used the observations of the Diffuse Infrared Background Experiment (DIRBE) on-board the *Cosmic Background Explorer* (COBE) as a reference for the absolute calibration of the diffuse light. The method is similar to that used for the calibration of the *AKARI* IRC All-Sky Survey (Pyo et al. 2010). If we assume that the sky brightness at mid-infrared wavelengths follows the blackbody spectrum (Leinert et al. 2002), the spectral energy distribution (SED) of the sky brightness $I_\nu(\lambda)$ can be written as

$$I_\nu(\lambda) = \tau B_\nu(\lambda, T), \quad (1)$$

where τ and T are the optical depth and the color temperature, respectively, and $B_\nu(\lambda, T)$ is the Planck function at the wavelength λ . The subscript ν in I_ν and B_ν means that the unit of brightness is given in the per-frequency unit. Use of a per-frequency unit is not a mandatory rule, but is done to follow the convention of adopting the unit of MJy in the previous ZL studies.

Our model SED, Equation (1), is a simple, empirical model and not a physically meaningful one. A physical model has to include i) the ZL integrated through a sophisticated IPD cloud model, ii) the integrated star light, iii) the diffuse Galactic light, and iv) the extragalactic background light (Leinert et al. 1998). For the absolute calibration, however, a detailed model of light sources is not necessary and an empirical

shape of SED suffices. Thus the temperature T in Equation (1) is not related to the temperature of the IPD, or of any other sources. On the other hand, Ootsubo et al. (1998, 2000) and Hong et al. (2009) modeled the infrared ZL spectra with the brightness integrals and suggested a two-temperature model of the IPD cloud in which the hot-dust component has a temperature of about 300 K or higher at 1 AU and the cold-dust component has a temperature of about 266 K or lower. But the hot-dust component is required to explain the part of the spectra at wavelengths shorter than $\sim 6 \mu\text{m}$ and a single component model is sufficient at longer wavelengths (Reach et al. 2003).

We have two unknown parameters, τ and T , in Equation (1). To fix these two parameters, the brightnesses at two wavelengths are sufficient; Pyo et al. (2010) used the DIRBE 4.9 and $12 \mu\text{m}$ bands to calibrate the *AKARI* All-Sky Survey at $9 \mu\text{m}$. In our case, we made use of the DIRBE 4.9, 12, and $25 \mu\text{m}$ bands, because the MIR-S and MIR-L channels cover the wavelength range from 7 to $24 \mu\text{m}$.

The DIRBE brightnesses were taken from the Calibrated Individual Observations (CIO) dataset³. For each *AKARI* MIR-S and MIR-L observation, we collected such DIRBE observations that satisfied the following conditions: i) The difference in the Earth’s heliocentric ecliptic longitude between DIRBE and *AKARI* observations is less than 5° and ii) the separation between the observing coordinates of the two observations is less than $\sim 10''$, half of the pixel size in the dataset. We collected the DIRBE observations for the MIR-S and MIR-L channels independently, because the lines-of-sight of the two channels are separated from each other (Figure 1). The mission period of the *COBE*/DIRBE was shorter than 1 year and the DIRBE observations were not available for five *AKARI* observations of IDs from 5121016-001 to 5121020-001. For each *AKARI* observation, about 20 sets of

³Available in the Legacy Archive for Microwave Background Data Analysis (LAMBDA) homepage (<http://lambda.gsfc.nasa.gov>) of the NASA.

DIRBE brightnesses were selected. We took the average of the selected brightnesses.

The DIRBE CIO dataset provides the quoted brightness in which the calibration assumed that the source spectrum follows $I_\nu \propto 1/\nu$. Because we assume a blackbody SED, we made the color correction on the DIRBE brightnesses, which depends on temperature only. For each set of three DIRBE brightnesses observed simultaneously, we determined the temperature T and the optical depth τ with the least-squares fit using the following model:

$$I_\nu^i = \tau B_\nu(\lambda^i, T) K^i(T),$$

where the superscript i runs over three DIRBE bands and I_ν^i , λ^i , and K^i are the quoted brightness, the effective wavelength, and the color-correction factor for the i -th band, respectively. The equation for calculation of the color-correction factor is given in Hauser et al. (1998a). The quoted and color-corrected DIRBE brightnesses and the fitting blackbody SED corresponding to the *AKARI*'s observation ID 5121021-001 are shown in Figure 3 for instance..

Once the temperature and optical depth were determined, we calculated the sky brightnesses at the MIR-S and MIR-L bands' reference wavelengths with Equation (1). The calculated brightnesses were divided by the ADU counts from the *AKARI* observations. Consequently, we obtained seven (MIR-S) or five (MIR-L) ratios between the calculated and measured brightnesses for each band and took their averages as the calibration factors. In Figure 3, the calibrated *AKARI* brightnesses are shown with green (for MIR-S channel) or red (for MIR-L channel) circles. The calibration factors used in this work are listed in Table 1.

The calibration factors for diffuse sky brightness are smaller than those for the point sources (Tanabé et al. 2008) by factors of about 0.85–0.89 for MIR-S bands and about 0.56–0.78 for MIR-L bands. The ratios between the diffuse and point source calibration factors are listed in Table 1. The difference of calibration factors between the point and

the diffuse sources is due to i) the point spread function (PSF) cut-off in the aperture photometry of the point sources and ii) the internal scattering and diffraction of light within a detector array (Arimatsu et al. 2011). The former causes the point source calibration factor to be overestimated, but does not cause a problem in point source photometry if a consistent aperture size is used for both the calibration and the photometry. On the other hand, the latter decreases the diffuse source calibration factor with respect to the “ideal” absolute calibration. As long as the internal scattering and diffraction are proportional to the incident brightness, our calibration method correctly takes them into account.

We note that our calibration factors are subject to the uncertainty in the absolute gain calibration of DIRBE, 3.0% at $4.9\mu\text{m}$, 5.1% at $12\mu\text{m}$, and 15.1% at $25\mu\text{m}$ (Hauser et al. 1998b). The uncertainties induce $\sim 10\%$ errors in our calibration. However, we will ignore those systematic errors because our central concern is to measure the fluctuation with respect to the sky brightness.

3. Seasonal Variation of the Sky Brightness

The sky brightness observed on the Earth-bound orbit changes with time due to the annual variation of the ZL (Deul & Wolstencroft 1988; Reach 1988; Vrtilik & Hauser 1995; Kelsall et al. 1998; Kwon & Hong 1998; Pyo et al. 2010). For detailed studies of the Solar system’s IPD cloud, such full models as those of Wright (1998) and Kelsall et al. (1998) are required. However, complete modeling of the IPD cloud is beyond the scope of this work. Instead, we tried simple sinusoidal fitting to the observed sky brightnesses, which assumes that the ZL at high ecliptic latitude is dominated by the smooth cloud component of the IPD cloud (Kelsall et al. 1998). The fitting function is given as a function of the Earth’s heliocentric ecliptic longitude, λ_{\oplus} , at the epoch of observation:

$$I_{\nu}(\lambda_{\oplus}) = a \sin(\lambda_{\oplus} - b) + c,$$

where a , b , and c are the amplitude, phase, and average brightness of the annual variation, and fitting parameters, respectively. In the fitting process, we fixed the period of the sine curve at 360° , which is a reasonable assumption. The results are plotted in Figure 4 and arranged in Table 3. For comparison, the results for the DIRBE 12 and $25\mu\text{m}$ bands observations are shown. The DIRBE NEP brightnesses are retrieved from the CIO dataset by collecting the observations pointing at an ecliptic latitude larger than 89.5° while avoiding the region within 0.5° of NGC 6543. The brightnesses within 5° intervals of the Earth’s heliocentric ecliptic longitude are averaged and shown in Figure 4 with gray triangles. Error bars are the statistical errors of the averages.

As can be seen in Figure 4 and in Table 3, the sine curves are good enough to describe the seasonal variation of the NEP brightnesses. The residuals after subtracting the fitting sine curves from the observed brightnesses are within $\sim 0.4\%$ of the average brightnesses for the *AKARI* observations. We plotted the residuals with respect to the Earth’s heliocentric ecliptic longitude, as shown in the right panels of Figure 4. A clear dependency of the residuals on the longitude was not found, which proves that a single sine function is good enough to describe the annual variation of the ZL towards the NEP. We note that the random residuals are caused by the variability of the IRC’s dark current, but not by the fluctuation of the sky brightness. The observed brightnesses and the fitting parameters in the S11 and L24 bands are, respectively, consistent with those in the DIRBE 12 and $25\mu\text{m}$.

Our observation fields deviated slightly from the exact position of the NEP, as shown in Figure 1. By the means of the IPD cloud model of Kelsall et al. (1998), we examined how much difference in brightness between the NEP and the *AKARI* Monitor Fields is introduced by the deviation. The model was evaluated for the NEP and the *AKARI* Monitor Fields at the observation epoch for each observation ID listed in Table 2, and then the difference between the two brightnesses was obtained. We calculated the model at the

wavelengths of the two IRC bands, S9W from MIR-S and L18W from MIR-L. To evaluate the model at the wavelengths of 9 and 18 μm , we turned off the inverse color-correction required to obtain the DIRBE quoted brightness. The emissivity modification factors at those wavelengths were obtained by logarithmically interpolating the values given in Kelsall et al. (1998). The Earth’s heliocentric coordinates required for the model calculation were retrieved from the HORIZONS ephemeris computation service operated by the Jet Propulsion Laboratory (JPL). The calculation results are shown in Figure 5(a).

The model calculation shows that the difference changes with time and is coupled with the solar elongation, one of the parameters most relevant to the ZL brightness. The solar elongation for the MIR-S and MIR-L channels at the *AKARI* observation epochs are plotted in Figure 5(b). Though the observing coordinates of the MIR-S channel are fixed at a celestial coordinates, the solar elongation slightly changes because the Earth revolves around the Sun. As can be seen in Figure 5, we have brightness dimmer than that of the NEP if the solar elongation is larger than 90° , and vice versa. In the case of the MIR-S channel, the difference becomes almost zero for the observation ID 5121021-001, at which the solar elongation is closest to 90° . For this channel, the brightness difference relative to the NEP is always smaller than or comparable to the standard deviation of the sinusoidal fitting residuals (Table 3). For the MIR-L channel, the moving line-of-sight in the celestial coordinates introduces another modulation to the solar elongation, in addition to that caused by the Earth’s motion. That results in solar-elongation deviation from 90° larger than that for the MIR-S channel; also, during the *AKARI* observation, the MIR-L channel fields maintain a solar elongation smaller than 90° . The sky brightnesses in the MIR-L fields are brighter than those at the NEP, but the difference is smaller than two times the standard deviation of the residuals after the sinusoidal fitting. Consequently, though the *AKARI* NEP Monitor observations were not pointed at the exact NEP coordinates, the observed brightnesses are almost the same as those of the NEP’s.

4. Fluctuation Analysis

We examined the fluctuation in the sky brightnesses observed in the six mid-infrared wavebands. To measure the fluctuation, we adopted the power spectrum method. We first subtracted the average pixel value from every valid pixel and filled blank pixels with zeros. We call this the fluctuation image, $\delta I(\mathbf{x})$, where \mathbf{x} is the pixel coordinates in units of radians. Then, the two-dimensional power spectrum image $P(\mathbf{k})$ is given by $P(\mathbf{k}) = |\delta I_k(\mathbf{k})|^2$, where \mathbf{k} is the two-dimensional wavenumber vector, and the fluctuation image's Fourier transform $\delta I_k(\mathbf{k})$ is defined as

$$\delta I_k(\mathbf{k}) = \frac{1}{L_x L_y} \int \delta I(\mathbf{x}) \exp(-i\mathbf{x} \cdot \mathbf{k}) d^2\mathbf{x}. \quad (2)$$

In Equation (2), L_x and L_y are the angular sizes of the image along x - and y -directions, respectively. To get the one-dimensional power spectrum $P(k)$, we took the average of $P(\mathbf{k})$ in which \mathbf{k} satisfies $k - \frac{1}{2}\Delta k \leq |\mathbf{k}| < k + \frac{1}{2}\Delta k$ after masking the pixel lines, $k_x = 0$ and $k_y = 0$. With an one-dimensional power spectrum, the fluctuation $F(k)$ at wavenumber k or, correspondingly, at scale $2\pi/k$ is given by (Thompson et al. 2007)

$$F^2(k) = \frac{L_x L_y}{(2\pi)^2} 2\pi k^2 P(k).$$

This method is usually used in the CNIRB studies (e.g., Kashlinsky et al. 2005; Thompson et al. 2007; Matsumoto et al. 2011).

We applied the method to the individual images and obtained 10 spectra for each of the MIR-S and MIR-L bands. The same method was applied to the dark frames. The fluctuation spectra of the sky brightness were obtained by quadratically subtracting the dark-frame spectra from those of exposure images. The sky fluctuation spectra are averaged after rejecting the largest and smallest values scale-wise, and are shown in Figure 6.

5. Discussion

At mid-infrared wavelengths the sky is very bright due to the ZL and the electron counts recorded in the IRC detector pixels are copious, usually larger than two thousands. Thus the photon noise is one of the major sources of fluctuation. To estimate the photon-noise contribution to the fluctuation, we artificially generated a pseudo-image filled with the values from a Poisson distribution. We generated 100 pseudo-images for each image, calculated the fluctuation spectra of the pseudo-images, and took the average over 100 spectra. The photon-noise fluctuation spectrum is individually calculated for each image because the sky brightness relevant to the photon noise changes with time, as discussed in Section 3. The average fluctuation spectrum of the photon noise is shown in each panel of Figure 6 with a gray line.

One of the sky brightness components that can be used to explain the fluctuation is the Galactic cirrus emission by interstellar dust. The fluctuation spectrum of the Galactic cirrus is known to have a power-law index in a range from 2.5 to 3.1 (Jeong et al. 2005; Miville-Deschênes et al. 2007). To evaluate the real fluctuation spectrum of the cirrus, we used the *AKARI* Far-Infrared Surveyor (FIS) observation of the NEP field (Matsuura et al. 2011) at a wavelength $90\,\mu\text{m}$. After removing the point sources, we measured the fluctuation of the image. To exclude the shot noise due to faint galaxies and the effect of large pixel size ($\sim 30''$), we used a fluctuation at scales larger than $85''$. Assuming that the structure of the Galactic cirrus is the same in other wavelengths, we converted the fluctuation measured at $90\,\mu\text{m}$ to the fluctuations in the mid-infrared bands by using the SED of the Galactic cirrus. Regarding the cirrus SED, we adopted the recent results from the *Herschel* and *Spitzer* observations by Compiègne et al. (2010). The cirrus fluctuation spectra are plotted in Figure 6 with magenta diamonds.

Another source of fluctuation is the shot noise due to faint sources. We estimated the

fluctuation F_{src} produced by the sources with flux fainter than the detection limit with the formula $F_{\text{src}} = \int S^2 (dN/dS) dS$, where S is the flux and dN/dS is the differential source count. The source count function is taken from the deep observations of the NEP with *AKARI* at $7\mu\text{m}$ (Wada et al. 2007). The detection limits of the MIR-S bands are shown in Table 1. For the MIR-L bands, the detection limits are not determined and the fluctuation caused by faint sources is not calculated. The fluctuation spectra of the faint sources in the MIR-S bands are drawn in Figure 6 with cyan dotted lines. Quadratic summation of the photon-noise, the cirrus, and the shot-noise spectra are also shown with black dashed lines. In Table 4, we arrange the fluctuations of dark current, sky brightness, photon noise, Galactic cirrus, and shot noise in six mid-infrared bands at the scale of $200''$.

The residual fluctuations at $200''$ after removing the photon noise, the Galactic cirrus, and the shot noise contributions from the sky-brightness fluctuations were calculated and are listed in Table 4. We note that the photon-noise contributions were individually subtracted from the corresponding sky-brightness fluctuations and then the photon-noise-removed fluctuations were averaged after rejecting the maximum and minimum values. The cirrus and the shot-noise contributions were subsequently subtracted. Subtracting operations were done in a quadratic sense, that is, we calculated the square-root of the difference between the squares of operands. The errors were properly propagated.

For the MIR-S bands, the fluctuations at the scales $\lesssim 100''$ were well described by the photon noise and the shot noise of faint sources. At larger scales, the slope of the spectrum becomes shallower, because the Galactic cirrus emission surpasses the fluctuation due to the photon and shot noises. Owing to polycyclic aromatic hydrocarbon (PAH) features, the cirrus emission is stronger in the short mid-infrared wavelengths than in longer wavelengths. The contribution of the cirrus emission decreases with the wavelength and becomes negligible in the MIR-L bands. The photon noise dominates the sky-brightness

fluctuation in the MIR-L bands at all the scales considered in this study. The residual fluctuation appears at scales larger than $100''$. At a few arcminutes scale, the residual fluctuation is detected at all mid-infrared bands except for the S7 band. One of candidates for the source of residual fluctuation at the mid-infrared wavelengths is the ZL. To verify this, observations towards various ecliptic latitudes are required in order to check the latitude-dependence of the residual fluctuation. In the current stage, we conclude that the residual fluctuations indicated in Table 4 are the upper limits of the ZL fluctuation. The most stringent upper limit at $200''$ scale is $\sim 0.02\%$ of the brightness at $18\ \mu\text{m}$. This limit is applicable to the ZL at near-infrared wavelengths, at which the sunlight scattered by the IPD particles is important (Matsumoto et al. 2011).

6. Conclusion

We made use of the *AKARI* IRC NEP Monitor Observations to examine the fluctuation in the sky brightness at the mid-infrared wavelengths. The fluctuation is measured by the power-spectrum method. After correction for the dark current, the fluctuation in the sky brightness is retrieved at six IRC mid-infrared bands. At wavelengths 7, 9, and $11\ \mu\text{m}$, the photon and shot noises dominates the fluctuation spectra up to the arcminute scale, while the Galactic cirrus component dominates above that scale. At longer wavelengths (15, 18, and $24\ \mu\text{m}$), the sky-brightness fluctuation spectra are comparable to the photon-noise spectra within a factor of two over a scale range from 5 to 200 arcseconds. Residual fluctuations are detected at scales larger than $100''$ at wavelengths larger than $7\ \mu\text{m}$ after removing the noise and cirrus contributions from the measured sky-brightness fluctuations. We take the smallest fluctuation, 0.02% of the sky brightness at the wavelength of $18\ \mu\text{m}$, as the upper limit of the sky-brightness fluctuation in the mid-infrared range.

This work is based on observations from *AKARI*, a JAXA project, with the participation of ESA. This work was achieved under the auspices of Prof. Seung Soo Hong. T.M. and S.M. were supported by Grants-in-Aid from the Japan Society for the Promotion of Science (18204018 and 21111004). This research made use of **PyRaf**, developed and maintained by the Space Telescope Science Institute (STScI). All figures in the paper were prepared with **matplotlib**, an open-source Python plotting library.

Facility: Akari (IRC)

REFERENCES

- Ábrahám, P., Leinert, C., & Lemke, D. 1997, *A&A*, 328, 702
- Arimatsu, K., et al. 2011, *PASP*, 123, 981
- Compiègne, M., Flagey, N., Noriega-Crespo, A., Martin, P. G., Bernard, J.-P., Paladini, R., & Molinari, S. 2010, *ApJ*, 724, L44
- Deul, E. R., & Wolstencroft, R. D. 1988, *A&A*, 196, 277
- Hauser, M. G., Kelsall, T., Leisawitz, D., & Weiland, J., eds. 1998a, COBE Diffuse Infrared Background Experiment (DIRBE) Explanatory Supplement, version 2.3, COBE Ref. Pub. No. 98-A (Greenbelt, MD: NASA/GSFC), available in electronic form from the NSSDC at http://lambda.gsfc.nasa.gov/product/cobe/dirbe_exsup.cfm
- Hauser, M. G., et al. 1998b, *ApJ*, 508, 25
- Hong, S. S., et al. 2009, in *Astronomical Society of the Pacific Conference Series*, Vol. 418, AKARI, A Light to Illuminate the Misty Universe, ed. T. Onaka, G. J. White, T. Nakagawa, & I. Yamamura (San Francisco: Astronomical Society of the Pacific), 29–38
- Jeong, W.-S., Lee, H. M., Pak, S., Nakagawa, T., Kwon, S. M., Pearson, C. P., & White, G. J. 2005, *MNRAS*, 357, 535
- Jeong, W.-S., et al. 2007, *Advances in Space Research*, 40, 600
- Kashlinsky, A., Arendt, R. G., Mather, J., & Moseley, S. H. 2005, *Nature*, 438, 45
- . 2007, *ApJ*, 654, L5
- Kelsall, T., et al. 1998, *ApJ*, 508, 44

- Kwon, S. M., & Hong, S. S. 1998, *Earth, Planets, & Space*, 50, 501
- Leinert, C., Ábrahám, P., Acosta-Pulido, J., Lemke, D., & Siebenmorgen, R. 2002, *A&A*, 393, 1073
- Leinert, C., et al. 1998, *A&AS*, 127, 1
- Lorente, R., Onaka, T., Ita, Y., Ohyama, Y., Tanabé, T., & Pearson, C. 2008, AKARI IRC Data User Manual Version 1.4, available in electronic form from the ISAS at <http://www.ir.isas.jaxa.jp/ASTRO-F/Observation>
- Matsumoto, T., et al. 2011, *The Astrophysical Journal*, 742, 124
- Matsuura, S., et al. 2011, *ApJ*, 737, 2
- Miville-Deschênes, M.-A., & Lagache, G. 2005, *ApJS*, 157, 302
- Miville-Deschênes, M.-A., Lagache, G., Boulanger, F., & Puget, J.-L. 2007, *A&A*, 469, 595
- Murakami, H., et al. 2007, *PASJ*, 59, S369
- Onaka, T., et al. 2007, *PASJ*, 59, S401
- Ootsubo, T., Onaka, T., Yamamura, I., Tanabé, T., Roellig, T. L., Chan, K., & Matsumoto, T. 1998, *Earth, Planets, & Space*, 50, 507
- . 2000, *Advances in Space Research*, 25, 2163
- Pyo, J., et al. 2010, *A&A*, 523, A53
- Reach, W. T. 1988, *ApJ*, 335, 468
- Reach, W. T., Morris, P., Boulanger, F., & Okumura, K. 2003, *Icarus*, 164, 384
- Santos, M. R., Bromm, V., & Kamionkowski, M. 2002, *MNRAS*, 336, 1082

Tanabé, T., et al. 2008, PASJ, 60, S375

Thompson, R. I., Eisenstein, D., Fan, X., Rieke, M., & Kennicutt, R. C. 2007, ApJ, 657, 669

Verdugo, E., Yamamura, I., & Pearson, C. 2007, AKARI FIS Data User Manual Version 1.3, available in electronic form from the ISAS at <http://www.ir.isas.jaxa.jp/ASTRO-F/Observation>

Vrtilek, J. M., & Hauser, M. G. 1995, ApJ, 455, 677

Wada, T., et al. 2007, PASJ, 59, 515

Wright, E. L. 1998, ApJ, 496, 1

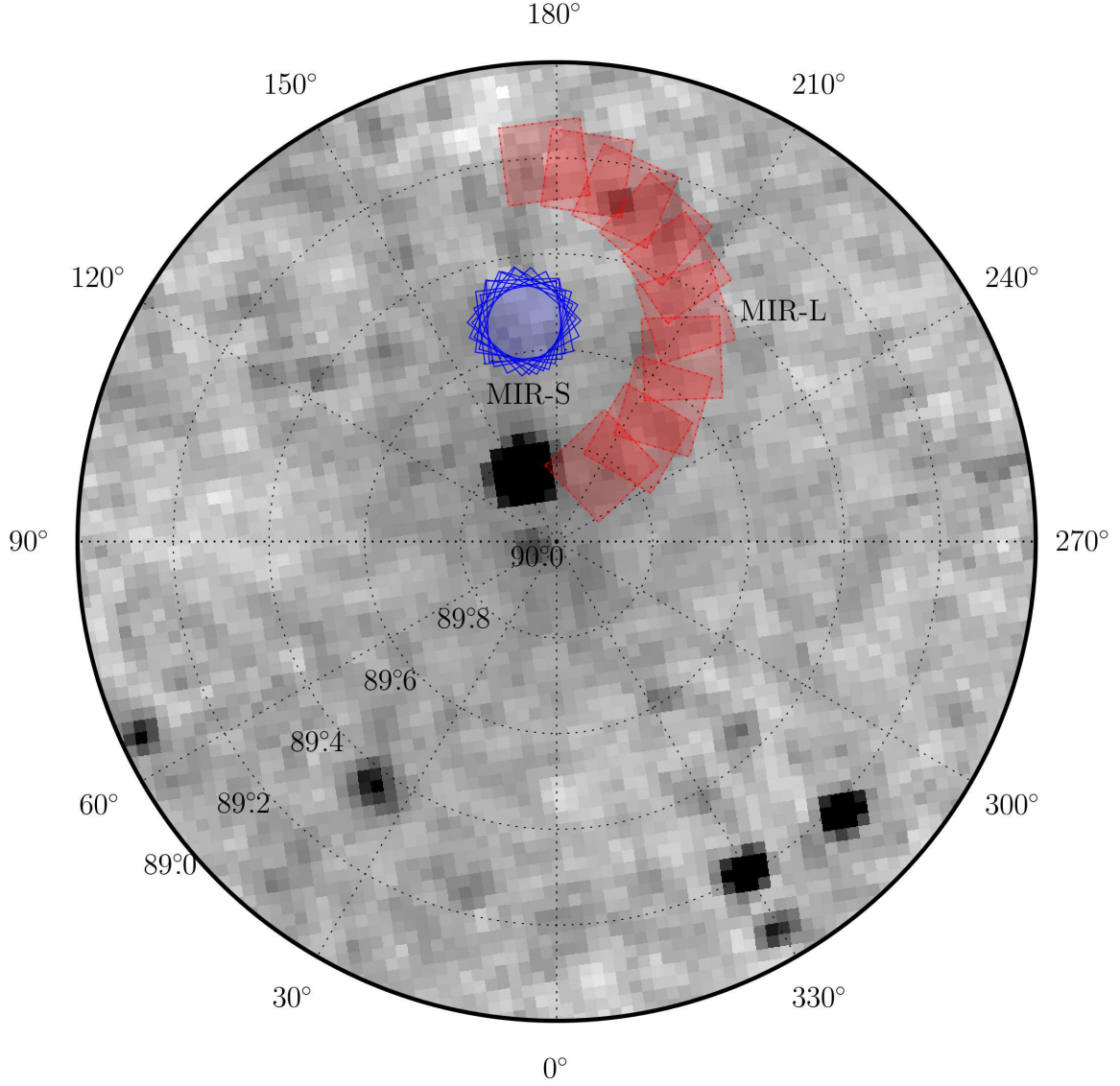


Fig. 1.— Monitor Fields in the ecliptic coordinates. The boxes with solid borders (colored blue) are the fields observed by the MIR-S channels, while those with dotted borders are the fields observed (colored red) by the MIR-L. The uppermost red box corresponds to the MIR-L field of observation ID 5121014-001, and the ID increases in the clockwise direction (ref. Table 2). The background image is from the Improved Reprocessing of the IRAS Survey (IRIS; Miville-Deschênes & Lagache 2005) Atlas at $12\,\mu\text{m}$ retrieved from the NASA/IPAC Infrared Science Archive. The center of the image is at the NEP, close to which the planetary nebula NGC 6543 is apparent. See the electronic edition of the Journal for a color version of this figure

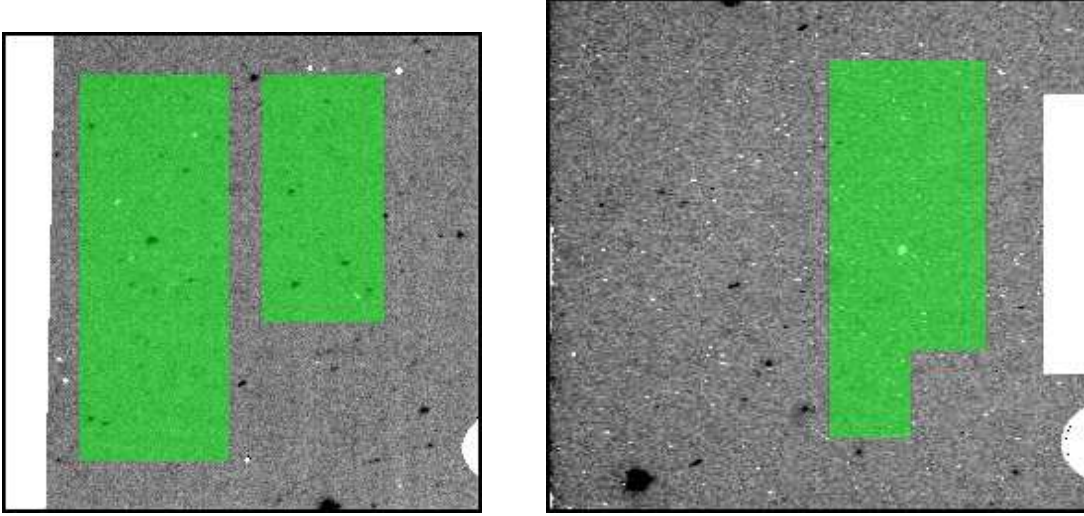


Fig. 2.— Regions (green-color areas) used in the analysis for the MIR-S (left) and MIR-L (right) channels. The background images are the real observations in the S9W and L18W bands after processing with the *AKARI* IRC image reduction pipeline for the observation ID 5121016-001. The images are inverted for visibility. Blank regions on the left (MIR-S), and right (MIR-L) sides in the frames are masked to measure the dark current. Small, circular areas on the right-bottom side are masked to avoid the emission from internal lamps. The sizes of images are scaled to match their angular scales. See the electronic edition of the Journal for a color version of this figure.

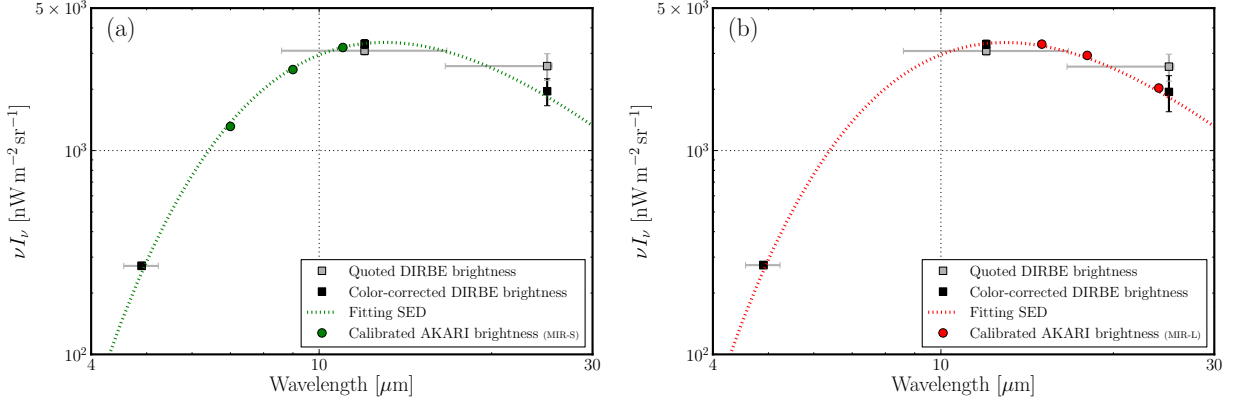


Fig. 3.— Calibration process for the MIR-S (a) and MIR-L bands (b). Data is plotted for the observation ID 5121021-001. Gray squares are the quoted DIRBE brightnesses at 4.9, 12, and 25 μm bands, corresponding to the *AKARI* observation configuration. The horizontal bars are the full-widths at half-maximum (FWHM) of the spectral response curves of the DIRBE bands, while the vertical bars are the errors in the DIRBE brightnesses due to the gain uncertainty (Hauser et al. 1998b). The black squares are the color-corrected DIRBE brightnesses based on the SED drawn with green (a) or red (b) dotted line. The SED is determined by fitting a blackbody SED to the quoted DIRBE brightnesses, while applying color-correction. Note that the SED curves and the DIRBE brightnesses in (a) and (b) are slightly different from each other, because the observing coordinates of the MIR-S and MIR-L channels do not coincide. Green (a) and red (b) circles are the calibrated *AKARI* brightnesses in the MIR-S and MIR-L bands, respectively. See the electronic edition of the Journal for a color version of this figure.

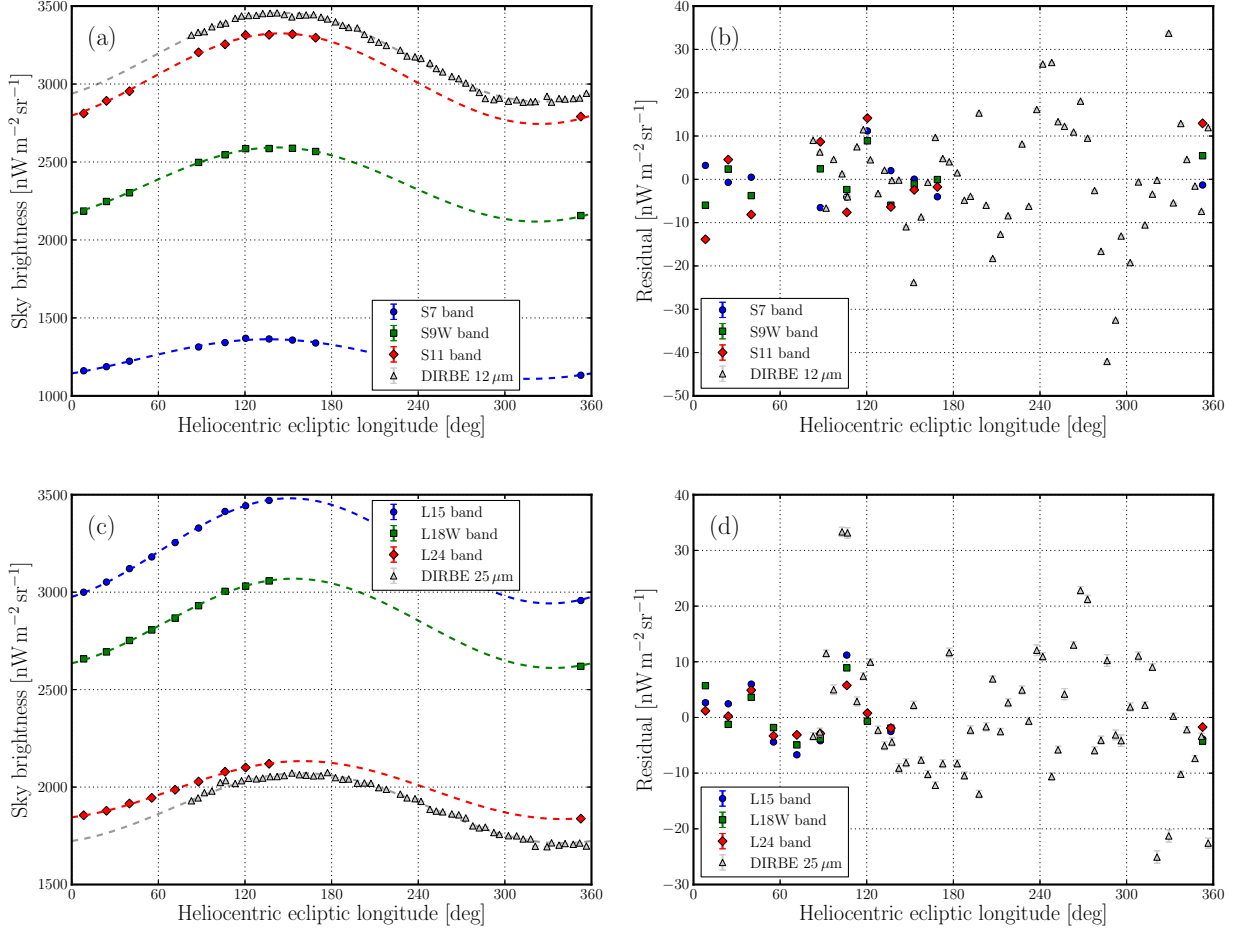


Fig. 4.— Sinusoidal fittings to the sky brightnesses observed by the *AKARI* NEP Monitor Observations (blue circles, green squares, and red diamonds) and the DIRBE observations (gray triangles). Panels (a) and (c) in the left column show the observed sky brightnesses (symbols) as functions of the Earth’s heliocentric ecliptic longitude and sine curves (dashed lines) fitting to the symbols. Panels (b) and (d) in the right column show the residuals after subtracting the fitting curves from the brightnesses. In each panel, we simultaneously plot the results for three bands of MIR-S and MIR-L channels in the top and bottom rows, respectively. The results for the DIRBE 12 and 25 μm are shown in the top and bottom rows, respectively, and drawn with gray points and lines. The error bar is drawn for each symbol, but it is too small to be apparent. See the electronic edition of the Journal for a color version of this figure.

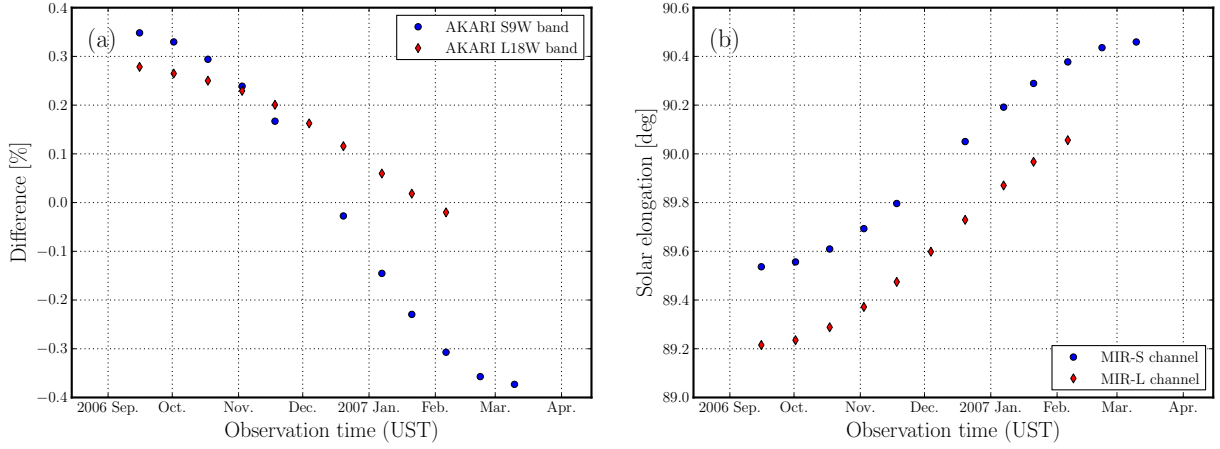


Fig. 5.— Difference in the ZL brightnesses between the *AKARI* NEP Monitor Field shown in Figure 1 and the NEP (a) and the variation of solar elongation (b) at the *AKARI* observation epochs. In panel (a), the differences are calculated by subtracting the brightnesses at the NEP from those at the Monitor Fields, and then dividing by the NEP brightnesses. The IPD cloud model of Kelsall et al. (1998) is evaluated to calculate the ZL brightness. In the panel, we plot the differences in the S9W (blue circles) and the L18W (red diamonds) bands. In panel (b), blue circles and red diamonds are for the MIR-S and MIR-L channels, respectively. See the electronic edition of the Journal for a color version of this figure.

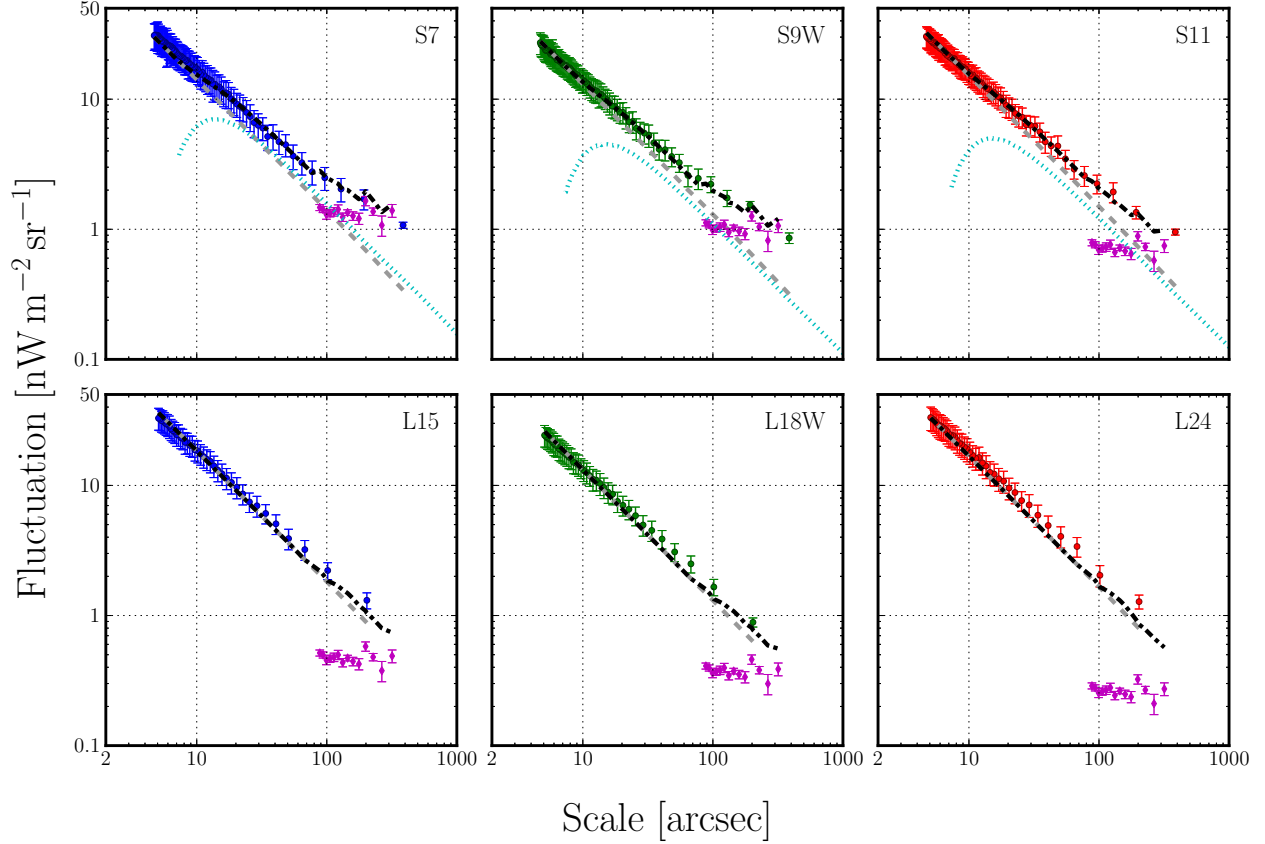


Fig. 6.— Fluctuation spectra of the mid-infrared sky brightness (colored circles), the photon noise (gray dashed lines), the Galactic cirrus (magenta diamonds), and the shot noise by unresolved faint sources (cyan dotted lines). The black dash-dotted lines are the spectra obtained by quadratically summing the fluctuation spectra of the photon and shot noises and cirrus. For MIR-L bands, the shot-noise fluctuation is ignored because the limiting magnitudes are not well determined. The error bars correspond to the statistical errors of the averages. See the electronic edition of the Journal for a color version of this figure.

Table 1. IRC Mid-infrared Channels and Photometric Bands

Channel	MIR-S			MIR-L		
Band	S7	S9W	S11	L15	L18W	L24
Wavelength [μm]	7	9	11	15	18	24
Bandwidth [μm]	1.75	4.10	4.12	5.98	9.97	5.34
Pixel scale ^a	$2''.34 \times 2''.34$			$2''.51 \times 2''.39$		
Field-of-view ^a	$9'.1 \times 10'.0$			$10'.3 \times 9'.5$		
$f_{\text{diffuse}}^{\text{b}}$ [$\text{nW m}^{-2} \text{sr}^{-1} \text{ADU}^{-1}$]	2.93	1.32	1.39	1.80	1.05	2.44
$f_{\text{diffuse}}/f_{\text{point}}^{\text{c}}$	0.86	0.89	0.85	0.75	0.78	0.56
5σ detection limits [μJy]	312	201	223

^across-scan \times in-scan

^bdiffuse source calibration factor

^cratio of the diffuse source calibration factor to the point source. f_{point} is taken from the 3rd column of Table 4.6.7 in Lorente et al. (2008).

Table 2. Observation Information

Obs. ID	Date Time (UST)	MIR-S		MIR-L	
		R.A.	Dec.	R.A.	Dec.
5121014-001	2006-09-15 17:06:14	17 ^h 55 ^m 23 ^s .1	66°37′55″.4	17 ^h 52 ^m 04 ^s .3	66°34′23″.8
5121016-001	2006-10-01 16:35:22	17 ^h 55 ^m 22 ^s .2	66°37′53″.4	17 ^h 52 ^m 20 ^s .5	66°29′10″.8
5121017-001	2006-10-17 16:07:25	17 ^h 55 ^m 21 ^s .3	66°37′49″.2	17 ^h 52 ^m 50 ^s .4	66°24′32″.4
5121018-001	2006-11-02 15:44:30	17 ^h 55 ^m 20 ^s .6	66°37′44″.5	17 ^h 53 ^m 32 ^s .1	66°20′51″.7
5121019-001	2006-11-18 00:33:04	17 ^h 54 ^m 20 ^s .3	66°18′29″.9
5121020-001	2006-12-04 00:17:29	17 ^h 55 ^m 15 ^s .6	66°17′29″.1
5121021-001	2006-12-20 00:06:37	17 ^h 55 ^m 20 ^s .3	66°37′26″.6	17 ^h 56 ^m 11 ^s .9	66°18′03″.9
5121022-001	2007-01-06 23:58:56	17 ^h 55 ^m 20 ^s .8	66°37′19″.1	17 ^h 57 ^m 10 ^s .6	66°20′31″.3
5121023-001	2007-01-20 23:56:09	17 ^h 55 ^m 21 ^s .4	66°37′14″.9	17 ^h 57 ^m 49 ^s .3	66°23′38″.9
5121024-001	2007-02-05 23:56:15	17 ^h 55 ^m 22 ^s .4	66°37′10″.7	17 ^h 58 ^m 22 ^s .8	66°28′13″.5
5121025-001	2007-02-21 23:59:52	17 ^h 55 ^m 23 ^s .3	66°37′09″.2
5121026-001	2007-03-10 00:06:48	17 ^h 55 ^m 24 ^s .3	66°37′08″.9

Table 3. Results of Sinusoidal Fitting

Channel	Band	a [nW m ⁻² sr ⁻¹]	b [°]	c [nW m ⁻² sr ⁻¹]	$\sigma_{\text{res}}^{\text{a}}$ [nW m ⁻² sr ⁻¹]
MIR-S	S7	126.93 ± 0.12	46.41 ± 0.08	1236.15 ± 0.12	4.91 (0.40%)
	S9W	237.74 ± 0.08	51.96 ± 0.03	2355.60 ± 0.09	4.86 (0.21%)
	S11	290.45 ± 0.09	54.45 ± 0.03	3034.43 ± 0.10	9.59 (0.32%)
MIR-L	L15	269.70 ± 0.13	61.12 ± 0.08	3211.98 ± 0.27	5.56 (0.17%)
	L18W	229.03 ± 0.10	63.56 ± 0.06	2840.21 ± 0.19	4.61 (0.16%)
	L24	148.60 ± 0.14	69.74 ± 0.14	1984.60 ± 0.27	3.25 (0.16%)
DIRBE	12 μm	284.86 ± 0.03	55.05 ± 0.01	3171.88 ± 0.03	13.73 (0.43%)
	25 μm	179.46 ± 0.13	69.58 ± 0.05	1891.68 ± 0.10	11.75 (0.62%)

^aStandard deviation of the residuals. Values in parentheses are the percentage of standard deviations with respect to the average brightnesses, c .

Table 4. Fluctuations at 200'' Scale^a

Channel	Band	Fluctuation [nW m ⁻² sr ⁻¹]					
		Dark current	Sky brightness	Photon noise	Cirrus ^b	Shot noise	Residual ^c
MIR-S	S7	0.80 ± 0.05	1.71 ± 0.30	0.71 ± 0.01	1.32 ± 0.03	0.82	...
	S9W	0.36 ± 0.02	1.54 ± 0.09	0.66 ± 0.01	1.01 ± 0.02	0.58	0.82 ± 0.18 (0.035%)
	S11	0.38 ± 0.02	1.35 ± 0.15	0.76 ± 0.01	0.71 ± 0.02	0.65	0.81 ± 0.30 (0.027%)
MIR-L	L15	0.25 ± 0.03	1.31 ± 0.18	0.88 ± 0.01	0.46 ± 0.01	...	0.89 ± 0.29 (0.028%)
	L18W	0.15 ± 0.02	0.89 ± 0.07	0.63 ± 0.01	0.37 ± 0.01	...	0.52 ± 0.13 (0.018%)
	L24	0.34 ± 0.04	1.28 ± 0.16	0.80 ± 0.01	0.26 ± 0.01	...	1.08 ± 0.22 (0.054%)

^aThe exact scale for the fluctuation measurements is 193''.05 for the MIR-S channel and 203''.31 for the MIR-L.

^bObtained by taking the average of the Galactic cirrus fluctuations between 100 and 300 arcseconds scales after rejecting the largest and the smallest values. Error is the statistical error of average.

^cValue in parentheses is the percentage of the fluctuation with respect to the average brightness (*c* in Table 3)

over the seasonal variation.